POLITECNICO
MILANO 1863

SCUOLA DI INGEGNERIA INDUSTRIALE
E DELL'INFORMAZIONE

Executive Summary of the Thesis

High-precision control optimization and validation of n-order Mach-Zehnder meshes for complex-values optical computing

Laurea Magistrale in Electronics Engineering

Author: Edoardo Mauri

Advisor: Prof. Marco Sampietro

Co-advisor: Alessandro di Tria

Academic year: 2024-2025

1. Introduction

Developments in the field of information technology have been strictly related to the evolution of the associated electronics circuits and systems, but this trend, along with Moore's law, is nearing its end. Applications such as Artificial Intelligence and data centers are growing in both dimension and complexity, pushing electronics to its physical limits. A cooperation between photonics and electronics is something no longer avoidable. Silicon photonics seems to be the perfect candidate for data-handling, and coherent meshes based on Mach-Zehnder interferometers (MZIs) have been proven capable of implementing complex-valued Matrix-Vector multiplications [1]. Each MZI can be modeled with the following transfer function:

$$T_{MZI} = je^{j\frac{\theta}{2}} \begin{bmatrix} sin(\frac{\theta}{2}) & cos(\frac{\theta}{2})e^{j\varphi} \\ cos(\frac{\theta}{2}) & -sin(\frac{\theta}{2})e^{j\varphi} \end{bmatrix} \qquad (1)$$

where φ and θ represent the phase shifts introduced by programmable actuators, used to implement a generic unitary transfer function.

However, the photonic alternative is not without challenges. Process non-idealities and environmental contributions strongly affect optics; thermal drifts or crosstalk change the behavior

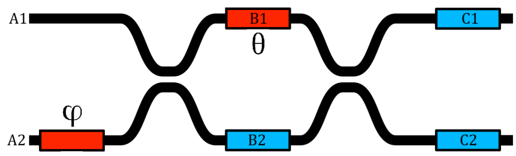

Figure 1: MZI schematic highlighting phase shifters and photodiodes

of optical components, resulting in an unreliable and unexpected result. The solution to these problems comes from the cooperation of both worlds. An optical mesh is used in combination with an electronic control layer in order to achieve, thanks to a specifically-designed control algorithm, a precise and stable behavior. It relies on transparent photodiodes to perform a run-time lossless measurement of light. The acquired signal is then processed, and the actuators are driven to achieve the desired result. The peculiarity of the system lies in its ability to extend the control to a generic n^{th} order matrix, without increasing the setup complexity for the single working point, but simply needing to implement multiple instances of the same structure. For reprogrammability purposes, the control was implemented by means of an *FPGA*, adopted to realize local feedback wherever is desired along the mesh.

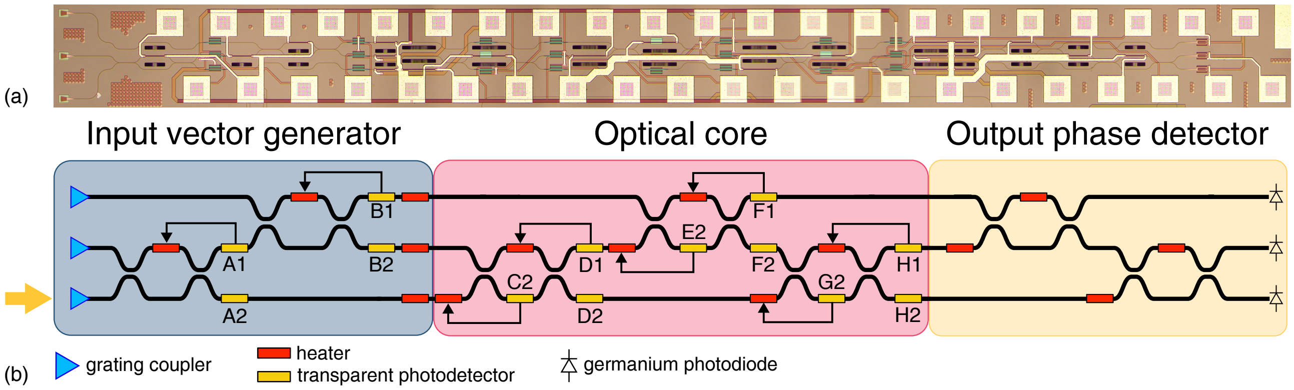

Figure 2: (a) Picture of the actual on-Silicon implementation of the structure, consisting of an input generator, an optical core and an output phase detector. (b) Schematic representation of the optical structure, highlighting photodiodes and heaters positioning.

The focus of this thesis is to validate and optimize the control on a 3×3 optical core, to show the scalability of the performances achieved with the previous implementation of a 2×2 structure. The results obtained show how a precise control in both amplitude and phase can be extended to a generic n^{th} order MZI mesh, paving the way for on-silicon optical computing.

2. Control strategy and 3x3 implementation

The core concept behind the algorithm is to perform the control locally in each Mach-Zenhder, thus avoiding the complexity of a global optimization of the whole system. This is performed by controlling the power split of each MZI in two points, in the middle branch between the two couplers and at the output.

We define the theoretical Power Split at a generic stage as a function of at least two readouts as follows:

$$PowSplit_{target}(X_i, X_j) = \frac{Pow_{X_i}}{Pow_{X_i} + Pow_{X_j}} \tag{2}$$

where $Pow_{X_{i,j}}$ is the optical power flowing in the upper and lower waveguide of the MZI, respectively. After choosing the target power split, the system acts on the heaters to force the light to interact in the two couplers in order to set $PowSplit_{target} = PowSplit_{measured}$.

Looking at Figure 1, and taking the first coupler as an example, we expect light to behave as follows:

$$PowSplit(B_2) = \frac{1}{2} + \frac{A_1 A_2}{A_1^2 + A_2^2} sin(\varphi + \xi) \tag{3}$$

where ξ is a generic phase difference between the inputs, and φ is the phase shift introduced by the input heater. Light after the second coupler will behave similarly, following a sinusoidal trend around half amplitude. Due to this sinusoidal shape, it is immediate to deduce that, by looking at Equation 3, choosing only the desired *PowSplit* is not enough to set a unique value of φ. For a given power split, two solutions can be identified for each period of the sinusoid, resulting in phase uncertainty. To address this issue, we exploit the derivative of the signal. It can be seen that, for the same power split, the sign of the derivative changes in the two points. By choosing the correct loop sign, we force the feedback loop to converge only to one of them, thus providing a complete description both in power and in phase.

The methodology adopted for the single MZI, which implements a 2×2 matrix, is then extended to a 3×3 mesh by composing three T_{MZI}.

$$T_{3\times3} = \begin{bmatrix} 1 & \\ & T_{MZI_3} \end{bmatrix} \begin{bmatrix} T_{MZI_2} & \\ & 1 \end{bmatrix} \begin{bmatrix} 1 & \\ & T_{MZI_1} \end{bmatrix} \tag{4}$$

Where each MZI has its own control loop, and the output of the matrix is the result of the composition of the single transfer functions implemented by each section.

The description of the system under exam, constituted by the optical core together with the structures necessary for a proper validation, is reported in Figure 2.b and is made up of the following blocks:

- *Input generator*: It has the task of generating the three components of the input vector. Starting from a single laser beam supplied from an external source at 1550 nm, a diagonal MZI structure is used to properly direct the light. We will call ψ_0 and ψ_2 respectively the phase shifters in between the couplers of the two MZIs.
- *Optical core*: 3×3 matrix implemented with Reck architecture, and thus relying on $\frac{N(N-1)}{2}$ MZIs, where N is the order of the matrix [3].
- *Coherent phase meter*: output structure relying on Germanium photodiodes to perform a phase measurement of the output vector.

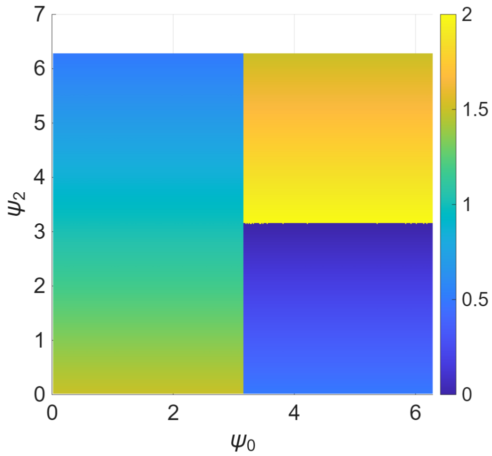

Figure 3: Phase difference χ_{12} $[rad]$ as a function of ψ_0 $[rad]$ and ψ_2 $[rad]$. A π phase step is visible along the ψ_0 direction, while instead along ψ_2 we can see a phase ramp proportional to half of the phase shift itself.

The two MZIs of the input generator can achieve any desired input power split by properly biasing their internal phase shifters. The resulting input vector, $IN = \left[A_1 e^{j\theta_1} \quad A_2 e^{j\theta_2} \quad A_3 e^{j\theta_3}\right]^T$, is then perfectly described and controlled in power, with a phase resulting from the chosen power splits.

The phase difference χ_{12} between the first two inputs, being at the output of a MZI, can only assume 0 or π as possible values, depending on the phase shift implemented by ψ_2. Instead, χ_{23} has a more complex description, being the result of the contribution of ψ_0 and ψ_2. In our setup, the input phase cannot be directly controlled; rather, it emerges as a natural consequence of the selected power splits. However, by carefully choosing the convergence derivative of the two actuators, the system can be constrained to lock the power split within a specific quadrant (see Figure 4).

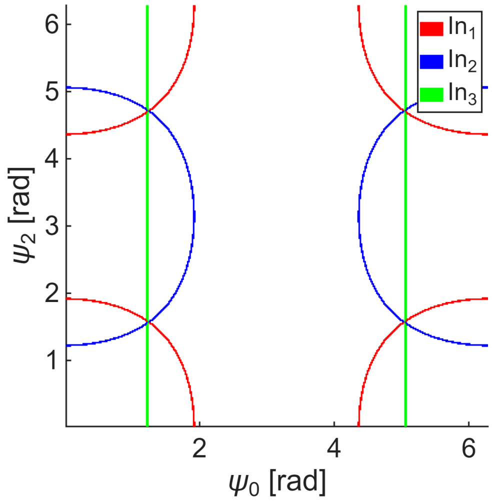

Figure 4: Four possible convergence points, each one corresponding to a different positioning in the phase map, corresponding to a 0.333 power split for each component of the input vector.

3. Electronic control chain

To implement the aforementioned control algorithm, a custom electronic acquisition system was developed to acquire and process signals and then feed them back to the chip to properly drive the phase shifters. The chip is mounted on a PCB named *Mantis*, which handles the necessary signal routing and preamplification to read from and actuate the device. The preamplification stage relies on Transimpedance Amplifiers (TIAs) with their virtual grounds directly connected to the cathodes of the photodiodes. The feedback resistors are tailored to the specific sensor type:

- *Transparent Photodiodes*: Due to the low photocurrent from these sensors, a 10 MΩ resistor is used in the TIA feedback, producing output signals ranging from 10s to 100s of mV. Along with a 1 pF feedback capacitance, it implements a 15.9 kHz pole.
- *Germanium Photodiodes*: given their higher responsivity, 10 kΩ feedback resistors are adopted for these sensors.

By means of ribbon cables, the Mantis PCB communicates with a motherboard. Here, an acquisition module receives and digitizes light readouts from the chip by using *Analog-to-Digital Converters (ADCs)*. The digitized signals are then processed by the FPGA, which performs all necessary signal processing tasks to properly evaluate the actuation voltage to be used. The actuation signals are then generated and sent back to the chip thanks to an actuation module, which also generates the needed supplies for the Mantis.

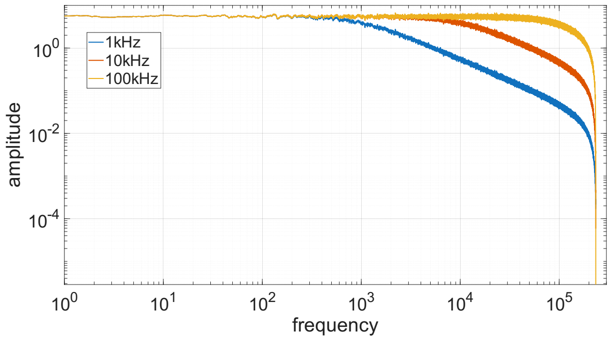

Figure 5: LPF simulation of the actual VHDL implementation with 3 different poles, taken with a decade of distance between them at: 1 kHz, 10 kHz and 100 kHz, showing the same in-band amplitude. It is also visible how the filter works properly up to its Nyquist frequency, which in our case is f_n=234 kHz.

Within the FPGA, two parallel acquisition chains are managed simultaneously, supporting two distinct operating modes for the integral controller:

- *PowSplit Mode*: The FPGA uses a digital normalized low-pass filter chain to extract the DC component from the incoming digitized signal (Figure 5). These DC values are used to evaluate real-time power splits across the mesh, which are then compared against user-defined targets.
- *Max/Min Mode*: The dithering technique is applied to extract the derivative from the incoming signal [4]. An integral controller then forces this derivative to zero to obtain either a maximum or a minimum of the transfer function, which is useful for calibration purposes.

A dedicated sign bit sets the correct loop polarity, allowing the system to distinguish between a maximum and a minimum, as well as between a positive and negative derivative.

4. Experimental results

An experimental characterization and operational validation is then performed on the previously presented system. The active control of the optical parameters is achieved via *titanium nitride (TiN)* thermal phase shifters (heaters) and non-invasive, surface-state absorption (SSA) transparent photodiodes. The optical signal is provided by a 1550 nm external laser source, coupled into the chip via grating couplers, with an optical power ranging between 7.5 dBm and 13 dBm.

4.1. Heaters characterization

The preliminary phase of the validation involves the electrical and electro-optical characterization of the TiN heaters. Using a Keithley 2450 Source Measure Unit (SMU), forced voltage sweeps were performed on devices of two lengths: 100 µm and 60 µm. Both heaters demonstrated Positive Temperature Coefficient (PTC) behavior, where resistance increases due to self-heating. The 100 µm heaters maintained stability up to an applied voltage of approximately 8.35 V. Beyond this threshold, the devices exhibited a sudden and irreversible decrease in resistance, indicating structural wear.

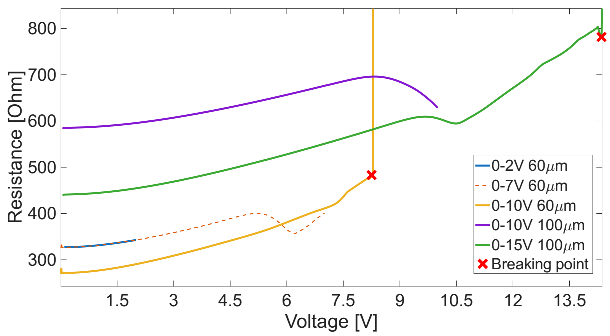

Figure 6: Resistance behavior over voltage for 100 µm and 60 µm TiN heaters. Multiple sweeps are performed with gradually increasing voltages in order to verify the operating limits of the actuators.

Similarly, the 60 µm heaters showed stable operation up to 4.5 V, with irreversible degradation beginning at 5.5 V. Optically, the heaters exhibited a precise linear correlation between the dissipated electrical power and the induced phase shift. To achieve a functional 3π phase shift, the 100 µm and 60 µm heaters required approximately 6.05 V and 4.3 V, respectively, remaining well within safety margins and thus ensuring predictable behavior.

4.2. Photodiodes non linearity

A critical aspect of the sensing validation involved assessing the non-linear responsivity of the transparent photodiodes.

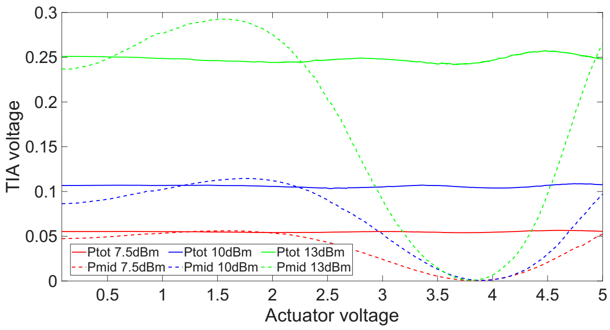

Figure 7: Internal power split with respect to the overall light power, measured for 7.5 dBm, 10 dBm and 13 dBm light sources.

Because these sensors rely on Surface-State Absorption (SSA), their response becomes highly non-linear under large optical powers. When subjected to a maximum optical signal of 13 dBm from the laser source, the internal MZI photodiode exhibited a significant overshoot, overestimating the power by approximately 17.26% compared to the overall average output power. This distortion was progressively mitigated by reducing the input power; the overshoot dropped to 8.86% at 10 dBm and further to a manageable 2.6% at 7.5 dBm. These findings dictated that optimal and reliable feedback control is achieved when the circuit operates at lower input optical powers.

4.3. Transparent phase measurement

Since directly extracting the optical phase along the internal waveguides without perturbing the system is not feasible using standard coherent receivers, a dedicated MZI was employed as a phase detector to accurately describe the generated input vectors [2]. By operating the first MZI of the optical core as a phase meter, the differential phase between coherent beams was measured. This operation was performed through a linear phase sweep at its input, with an overall Root Mean Square (RMS) error of 3.4% compared to theoretical simulations.

This phase meter configuration allowed for the generation of a three-dimensional phase map, linking specific input power combinations directly to phase shifts derived from the heater voltages of the input MZIs (Figure 9).

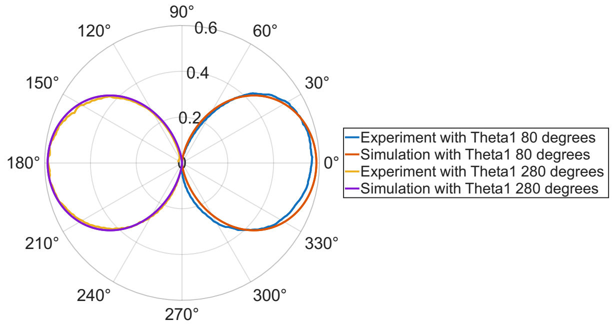

Figure 8: Polar plot showing a comparison between simulated and experimental results, of two π long phase measurements along a bell-shaped function. A maximum amplitude error of 4.5% and an RMS phase error of 3.4% were measured.

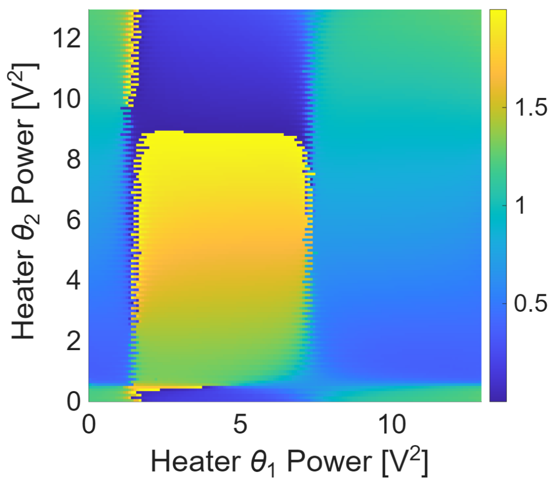

Figure 9: Three dimensional experimental result of MZI_1 input phase. An offset is present in the origin along both directions with respect to the simulation results due to non-ideality of the physical implementation.

4.4. Matrix-vector multiplication validation

The final validation focuses on the full matrix setting and Matrix-Vector Multiplication (MVM), conducted through two complementary methodologies to verify computational precision:

- *Discrete State Validation*: The 3x3 matrix was electronically locked to a specific target transfer function, calculated by the control software as a function of the chosen phase shifts, and its fidelity was tested against eight distinct input vectors at an optimized power of 1 dBm from the detector. The experimental power splits along the mesh closely matched the theoretical predictions, producing modest RMS errors bounded between 1.12% and 5.69% with the control paused after a preliminary setting. When the input optical power was increased to about 4 dBm, the precision degraded, showing RMS errors up to 6.8%. This corroborated the destructive impact of photodiode non-linearities at higher light intensities. The maximum deviations observed in *PowSplit* E_2 were primarily due to the topological impossibility of experimentally measuring the phase difference between the first two inputs, which instead had to be theoretically estimated via simulation. It is important to note that, in both cases when the control is active, our feedback is able to set a power split that deviates by less than 0.003% from the desired one.

PowSplit	RMS %Error (1 *dBm*)	RMS %Error (3.76 *dBm*)	Δ
C2	1.96	2.93	0.97
D1	2.02	1.46	-0.56
E2	5.69	6.81	1.12
F1	2.89	3.34	0.46
G2	1.12	1.38	0.26
H1	1.41	2.34	0.93

Table 1: Comparison and variation of RMS errors between the two configurations. An overall higher percentage error is present for the highest power setting.

- *Extensive Error Map Generation*: An arbitrary matrix was electronically fixed as in previous point. A comprehensive validation was then executed by performing a continuous linear sweep of the input phase actuators across a dense grid of 22,500 distinct operational points over a 40-minute span. The post-processed data revealed a behavior similar to previous measurements for MZI_1, where the input phase description was highly precise, and for MZI_2, although with a slightly worse accuracy. However, the final computational stage (MZI_3) exhibited a pronounced degradation in accuracy. This amplified error at the mesh's output provided empirical proof of the sequential accumulation of the errors due to a non perfect input phase description in previous stages, which were further exacerbated by thermal cross-talk and inevitable temporal drifts sustained during the prolonged measurement.

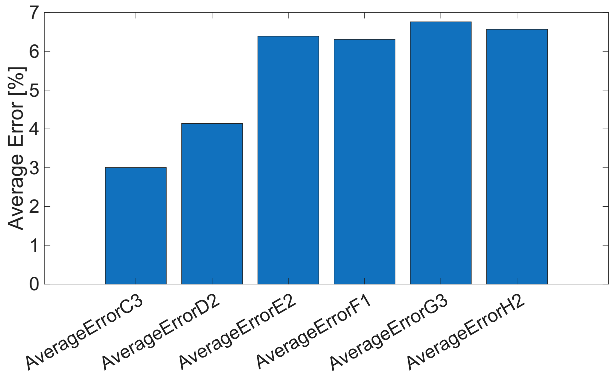

Figure 10: Histogram showing the average of the error modules for each power split of the matrix.

5. Conclusions

In conclusion, this thesis successfully validated an FPGA-based control system for a 3x3 coherent optical mesh, marking a crucial step toward complex-valued photonic computing. Experimental characterization defined the operational limits of TiN thermal actuators and demonstrated the necessity of operating at low optical powers (1 dBm) to mitigate photodiode nonlinearities. Although validations confirmed high system fidelity with RMS errors between 1 % and 6 %, the sequential error accumulation and thermal cross-talk in the final stages indicate that future developments must focus on a better phase description for the input vector and a new system configuration where the control is kept active during computation, to fully appreciate the accuracy capabilities of the control system.

References

[1] Wim Bogaerts et al. Programmable photonic circuits. *Nature*, 586(7828):207–216, 10 2020.

[2] Alessandro di Tria et al. High-precision automated setting of arbitrary magnitude and phase of mach–zehnder interferometers for scalable optical computing. *Laser & Photonics Reviews*, 20(2):e00610, 2026.

[3] M. Reck et al. Experimental realization of any discrete unitary operator. *Physical review letters*, 73(1):58, 1994.

[4] Francesco Zanetto et al. Dithering-based real-time control of cascaded silicon photonic devices by means of non-invasive detectors. *IET Optoelectronics*, 15(2):111–120, 2021.